Pattern Formation in Confined Core-Shell Structures: Stiffness, Curvature, and Hierarchical Wrinkling

Ji Hoon Kim, Jung Gun Bae, Hyunsik Yoon, and Won Bo Lee*

Adapting sheets to doubly curved surfaces is a longstanding challenge in various engineering disciplines, from flexible and stretchable electronics to the automotive industry. However, current understanding often focuses on specific scenarios and neglects the diverse range of substrate conditions encountered in nature. This study investigates the pattern formation in confined core-shell structures by modulating the levels of stiffness and curvature of the substrate. Beginning with the Föppl–von Kármán equation, this theory uncovers how the degree of confinement determines the location of wrinkles within confined sheets. Furthermore, the synchronization of patterns is observed: the formation of dimple or buckyball patterns on curved surfaces simultaneously with hierarchical wrinkles due to boundary constraints. The analytical models elucidate these phenomena, and both macroscopic and microscopic features can be systematically engineered to align with quantitative predictions. This research expands the current understanding of the sheet conformation problem and paves the way for pattern engineering across a range of curved structures.

1. Introduction

The challenge of conforming sheets to doubly curved surfaces has intrigued researchers in multiple disciplines, including wearable technology,[1–3] flexible electronics[4–10] and medical

J. H. Kim, W. B. Lee
Department of Chemical and Biological Engineering
Seoul National University
Seoul 08826, Republic of Korea
E-mail: wblee@snu.ac.kr

J. G. Bae, W. B. Lee
School of Chemical and Biological Engineering
Institute of Chemical Processes
Seoul National University
Seoul 151-742, Republic of Korea

H. Yoon
Department of Chemical and Biomolecular Engineering
Seoul National University of Science and Technology
Seoul 01811, Republic of Korea

implants.[11,12] Central to this conundrum is Gauss's Theorema Egregium, which explains that planar sheets cannot conform to curved surfaces without frustration.[13] Previous solutions to this challenge have often involved encapsulating spheres using different complex shapes.[14–16] For flat disks, efforts have focused on determining the extent of the wrinkled region and using the degree of confinement as a key metric to clarify the compatibility problem. In particular, the investigations conducted so far have focused primarily on specific scenarios, such as when the substrate is either in a liquid state, such as in the sheet-on-droplet problem,[17–20] or when the substrate is highly rigid and experiences minimal deformation.[21–23] However, this narrow focus has neglected a wider range of substrate mechanical properties that could be exploited in practical applications.[24,25]

Here, we present a diagram depicting the patterns of metal sheets confined to pre-polymer droplet substrates by manipulating the curvature and moduli of the substrate. Beginning with the Föppl–von Kármán (FvK) equations, this study investigates how the degree of confinement determines macroscopic features (e.g., unwrinkled length) using far-from-threshold theory and experiment. Thermal stress, applied during the metal deposition step by thermal evaporation, acts as an additional factor that increases the degree of confinement. This additional stress leads to a range of outcomes, from the coexistence of unwrinkled regions and radial wrinkles, as documented in geometrically incompatible confinement studies,[23,26–28] to complex patterns in core-shell microspheres.[29–33] Additionally, a new type of pattern synchronization is observed, consisting of either dimple or buckyball patterns on curved surfaces decorated with hierarchical wrinkles at the edges. Starting from the scaling law proposed by Cerda and Mahadevan,[34] we derive scaling laws to describe microscopic features (e.g., wavelength) using energy balance and theories associated with the wrinkling cascade.[35,36] Our experimental findings demonstrate a robust correlation with these derived scaling laws. This novel pattern engineering on curved surfaces offers promising opportunities for practical implementation in various engineering domains, including wearable technology, flexible electronics, and medical prostheses.

**ADVANCED
SCIENCE NEWS**

www.advancedsciencenews.com

**ADVANCED
MATERIALS
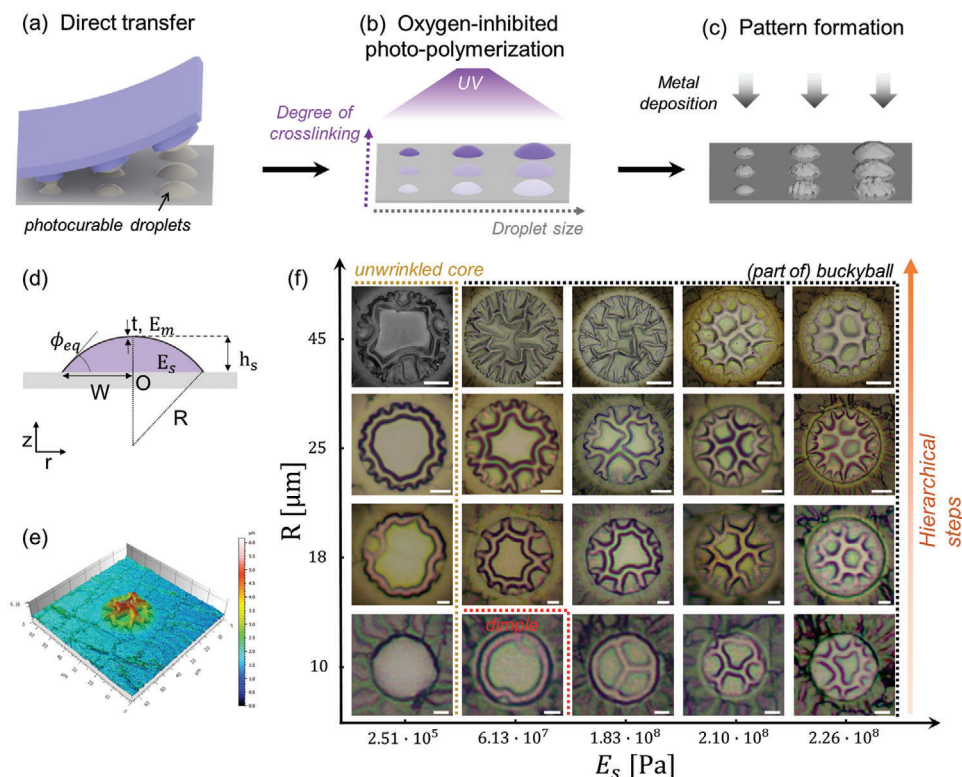INTERFACES**
Open Access

www.advmatinterfaces.de

Figure 1. Pattern formation within confined core-shell structures. Experimental schematic is shown in (a–c): a) Direct transfer of liquid droplets on the substrate. b) Modulation of κ and E_s of the droplets by adjusting the dimensions of the direct transfer step and τ. While depicted as varying in size and properties on a single substrate for clarity, the uniform microstructures are arrayed over a large area, as shown in Figure S4 (Supporting Information). c) Pattern formation induced by metal film deposition. d) Dimensions of the sheet-on-drop configuration. e) A 3D image characterized by a confocal microscope ($E_s \cong 2.10 \times 10^8$ Pa, $R \cong 25\mu m$) f) Phase diagram depicting the patterns of metal sheets on spherical cap-shaped substrates as a function of the parameters R and E_s. The scale bars corresponding to $R = 10, 18, 25, 45\mu m$ are 2, 2, 5, and 10μm, respectively.

2. Results and Discussion

The experimental schematic and morphological diagram for pattern formation is depicted in **Figure 1**. Initially, photocurable oligomers (precursor of polyurethane acrylate, PUA) were uniformly dispersed as microdroplets on a substrate using the direct transfer method,[37] as illustrated in Figure 1a. By fine-tuning the dimensions of the micropillar stamp and the thickness of the spin-coated film, we achieved precise control over the droplet size and, consequently, their curvature (κ). The degree of cross-linking within these droplets was modulated by varying the UV curing time (τ), as illustrated in Figure 1b. Throughout this process, oxygen inhibition in photo-polymerization[38] was strategically leveraged to decelerate the curing rate, thereby facilitating nuanced control over the degree of cross-linking as a function of τ. To estimate the effective Young's modulus of the substrate (E_s) for each τ, we employed a well-established scaling relationship,[34] $\lambda \approx t(E_f/E_s)^{1/3}$. Given that the τ versus E_s profile is influenced by the Damköhler number ($Da \equiv \varphi\epsilon[PI]I_0L^2/D_O[O_2]_0$),[38] we designed a flat PUA-Al bilayer system with a comparable Da to that of the curved bilayer ($Da_{flat}/Da_{curved} \approx 1.15$ for $R = 25 \mu m$). We used the measured wavelengths (λ_0) of the 2D stochastic wrinkle pattern on this planar system, obtained by fast Fourier transform (FFT) analysis of captured images, to estimate E_s for each τ using the scaling law

(Figures S1 and S2, Supporting Information). We used a thermal evaporator to deposit an aluminum film on spherical cap-shaped droplets, characterized by regulated values of radius of curvature (R) and E_s (Figure 1c). In this step, deformation occurs when the aluminum film is deposited onto thermally expanded droplets, as illustrated in Figure S3 (Supporting Information). This methodology has reliably produced uniformly patterned microstructures (approximately $10^4 \#/cm^2$, representative images in Figure S4, Supporting Information). The uniformity and proliferation of these structures under various experimental conditions confer substantial statistical advantages to our investigation, as they mitigate the uncertainties associated with measurement such as λ. Figure 1d visually presents the initial configuration dimensions, while Figure 1e exhibits a representative 3D confocal image for a comprehensive verification of the 3D structure. Figure 1f showcases our extended experimental results in the form of a phase diagram illustrating the acquired morphologies. The Young's modulus of the substrate $2.51 \times 10^5 \leq E_s \leq \times10^8$ Pa, and the radius of curvature $10 \leq R \leq 50\mu m$ were adjusted within these specified ranges. The metal thickness (t) was maintained at 20 nm, and the equilibrium contact angle (θ_{eq}) of the PUA oligomer on the PDMS was consistently measured at about 25° across all experimental conditions. Other constants in this system are detailed in Table S1 (Supporting Information).

Analyzing the morphological diagram from a qualitative perspective, it is clear that variations in E_s, R, or the well-established dimensionless parameter $C_s = (E_s/E_f)(R/t)^{1.5}$[30,32,33] distinctly influence λ, the number of hierarchical steps, the unwrinkled length, and the wrinkle types.

To theoretically elucidate these dependencies, we begin with the axisymmetric FvK equations in the "tension-field" limit $(t \to 0)$:[17,23,26,39]

$$\sigma_{rr}\zeta_0'' + \frac{\sigma_{\theta\theta}\zeta_0'}{r} - K_s(\zeta_0 - \zeta_{sp}) = 0 \tag{1}$$

$$\partial_r(r\sigma_{rr}) = \sigma_{\theta\theta} \tag{2}$$

here, σ_{rr} and $\sigma_{\theta\theta}$ refer to the radial and azimuthal stresses, and ζ_{sp} and ζ_0 represent the axisymmetric initial shape and the non-oscillatory asymptotic shape of the sheet,[22] respectively. The first and second equation represent force equilibrium in the radial and vertical directions, respectively. We employed Winkler's restoring force ($=-K_s(\zeta_0 - \zeta_{sp})$) as the model for the normal external force (P). Despite the system containing uncured oligomers in the liquid state, we chose to utilize a Winkler substrate with stiffness ($K_s = E_s\sqrt{Rt}$),[40] as opposed to previous studies applying Laplace pressure for P ($=2\gamma/R$).[17,20] The rationale behind this choice is that the key scaling results of the sheet-on-liquid drop problem exhibit distinct deviations compared to the morphological changes in our system (refer to 'p evaluation' section of the Supporting Information for related discussion). Furthermore, our system is situated within the domain of high bendability, as indicated by the condition $\epsilon^{-1} = \gamma W^2/B \gg 1$,[17] rendering the bending term negligible in the force balance of the dominant terms. In preceding investigations of situations where the sheet is barely deformed (for large K_s), the approximation $\zeta_0 \approx \zeta_{sp}$ is commonly employed.[22,23,26] Conversely, when K_s is minimal, the substrate is significantly deformed beneath the sheet,[17,26] leading to $\zeta_0 \to 0$. Extending from these concepts, we have newly proposed the generalized approximation relationship connecting ζ_0 and ζ_{sp}, which can be articulated as follows:

$$\zeta_0(r) \approx (1-p)\zeta_{sp}(r) \tag{3}$$

here, p denotes a newly defined parameter associated with the degree of deformation within the interval (0, 1) (detailed procedures in 'p evaluation' section and Figure S5, Supporting Information). The introduction of p allows for the consideration of a relatively large deformation which is not covered by the published work of Davidovitch and Hohlfeld,[26] where the derivation is progressed under a low deformability assumption ($\zeta_0 \approx \zeta_{sp}$). By combining Equation (1) and (2) with fundamental relationships involving σ, ϵ, u, ζ, we derive the confinement parameter α in our system as follows:

$$\alpha \equiv \frac{p^2}{8}\frac{Y}{\gamma}\sin^2\phi_{eq}(1-\cos\phi_{eq})^2\left(\frac{E_s}{E_f}\right)^2\left(\frac{R}{t}\right)^3\frac{1}{(1-q)^2} \tag{4}$$

γ denotes the surface tension induced by the difference in surface energies between a metal interfaced with a substrate and PDMS,[41] and $Y = E_f t$ represents the stretching modulus. The established correlation, akin to well-studied systems like sheets
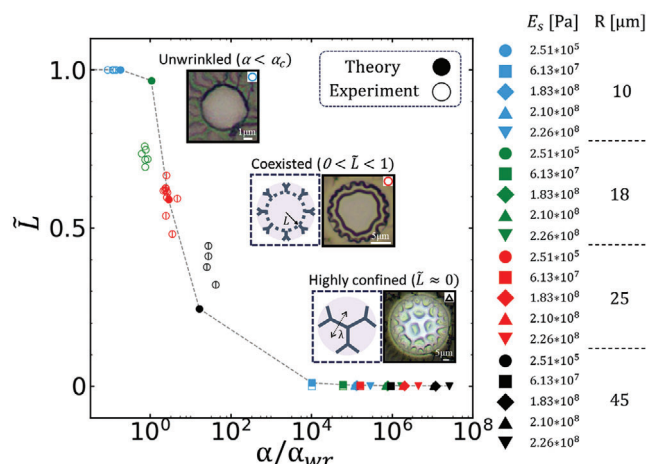

Figure 2. Influence of α on the macroscopic feature, $\tilde{L}$. A comparison between experimental and theoretical values illustrates the relationship between the normalized parameter $\tilde{L}$ and α/α_{wr}. Schemes for defining the unwrinkled length L are also incorporated. Regions where dimples or part of polygons are observed are consistently considered as having $\tilde{L} \approx 0$. The theoretically obtained values are displayed as discrete points rather than curves because the values of p and q are obtained discretely.

on foundations or indentation problems,[18,19,37] delineates a direct proportional relationship between the parameter α and the ratio of geometrical strain ($\approx\sin^2\phi_{eq}(1-\cos\phi_{eq})^2$) to mechanical strain ($\approx\gamma/Y$). This relationship also includes the square of the value of C_s, a quantifiable metric for pattern selection in core-shell spheres.[32] Parameter q is defined as $q \equiv 1 + \epsilon_0(1-\nu)$ and correlates with thermal strain,[42] where ϵ_0 corresponds to the thermal strain in a flat Al-PUA bi-layer system (details of 'q evaluation' in Figures S6 and S7, Supporting Information). In essence, in addition to the geometrical strain induced by curvature, ϵ_0 resulting from the mismatch in thermal expansion during metal deposition processes[43] acts as an additional form of geometrical strain, which operates in a manner that accentuates the augmentation of α.

This α is derived from the expansion of the leading terms in the FvK equations ($O(f^0)$), thereby establishing a correlation with the macroscopic feature, specifically the unwrinkled length L. By differentiating between the inner core and unwrinkled zone ($0 < r < L$) and the outer wrinkled zone ($L < r < W$), and utilizing the matching conditions of these two zones along with the effective confinement parameter $\bar{\alpha}$ in the unwrinkled zone (which equates to a critical value $\alpha_{wr}^0 \approx 4$),[17] a relationship between α and L can be derived as follows:

$$\frac{\alpha}{\alpha_{wr}^0} = \frac{\tilde{L}^{-2}}{1-\tilde{\sigma}_0}(\tilde{L}^{-1} - \tilde{\sigma}_0) \tag{5}$$

In this context, $\tilde{L} = L/W$ and $\tilde{\sigma}_0 \approx (Y/\gamma)(1-q)/(1-\nu)$ denote normalized L and thermal stress induced during metal deposition, respectively. Both this relation and experimental data have been plotted in **Figure 2**. As indicated by this equation, it is evident that when $\alpha < \alpha_{wr}^0$, the system exists in an unwrinkled state, and with increasing α, $\tilde{L}$ decreases. These cases are prominent for $E_s \cong 2.51 \times 10^5$ Pa (for uncured droplets), where α is not sufficiently large, resulting in the presence of an

unwrinkled zone. These results align remarkably well with previous sheet-on-droplet problems.[20,37] For oligomer droplets, even slight progress in curing induces a rapid escalation in E_s, leading to a corresponding significant increase in α. This incremental shift causes $\tilde{L} \to 0$, as deduced from Equation (5), which also aligns well with the previously observed outcomes of pattern formation in the microspheres (with large κ).[30–32] Consequently, this relationship proves to be a universal bridge, encompassing the conformation of sheets onto liquid substrates and the buckling behavior of core-shell microspheres.

Continuing from the exploration of macroscopic features discussed earlier, we now shift our focus to the analysis of microscopic features. Within core-shell structures, the transitions observed in morphologies–spanning from dimples to buckyballs and labyrinth patterns–have been extensively investigated in terms of parameters such as R/t, E_f/E_s, and excess stress.[14,31] Hence, instead of aiming to replicate these morphological transitions, our emphasis lies in estimating λ of the bulk region (where the boundary effect is negligible) and quantitatively understanding the variation in radial wavelength resulting from the confined edge effect. To initiate this analysis, we draw upon the universal law proposed by Cerda and Mahadevan:[34]

$$\lambda = 2\pi \left(\frac{B}{K_{eff}}\right)^{1/4} \qquad (6)$$

where K_{eff} signifies the effective stiffness of the substrate. Subsequently, Paulsen et al.[22] investigated this universal law under tension and for curved surfaces, where they established that $K_{eff} = K_s + K_{curv} + K_{tens}$ with curvature-induced stiffness $K_{curv} = Y\zeta_0''^2$ and tension-induced stiffness K_{tens} is defined as $K_{tens} = \sigma_{rr}(\Phi'/\Phi)^2$. Here, $\Phi \equiv mf$ represents the excess hoop strain absorbed by wrinkles, a parameter employed within the slaving condition. For large α, K_{curv} dominates other stiffness terms within the bulk region. Leveraging this approximation, it yields:

$$\frac{\lambda}{R} \sim \left[\left(\frac{E_f}{E_s}\right)^2 \left(\frac{t}{R}\right)^5\right]^{1/4} \qquad (7)$$

In this context, details related to the derivation and the underlying assumptions are provided 'λ calculation' section in the Supporting Information. To validate this scaling relation, λ was acquired under diverse experimental conditions and subsequently fitted to **Figure 3**. We employed the definitions illustrated in Figure 3a to evaluate λ for dimple or (part of) buckyball patterns. Regarding dimples, the diameter was considered as λ, whereas for (part of) buckyballs, the distance between centers of mass was directly assessed or the polygon area was employed to estimate λ (assuming the polygons take the shape of hexagonal shape and each vertex connected to three intersecting line segments). To enhance the accuracy of these measurements, we utilized statistical image processing techniques, including circle and particle detection, to mitigate measurement uncertainties (Figure S8, Supporting Information). The well-fitted outcomes indicate that λ displays greater sensitivity to κ compared to the modulus ratio (E_f/E_s). In contrast to K_s and K_{curv}, which are independent of r, the parameter K_{tens} is a function of r (indeed, K_{curv} also exhibits a weak dependence on r, but this dependency is assumed negligible based on the assumption $\gamma \ll \sigma_0$). For the sub-dominant
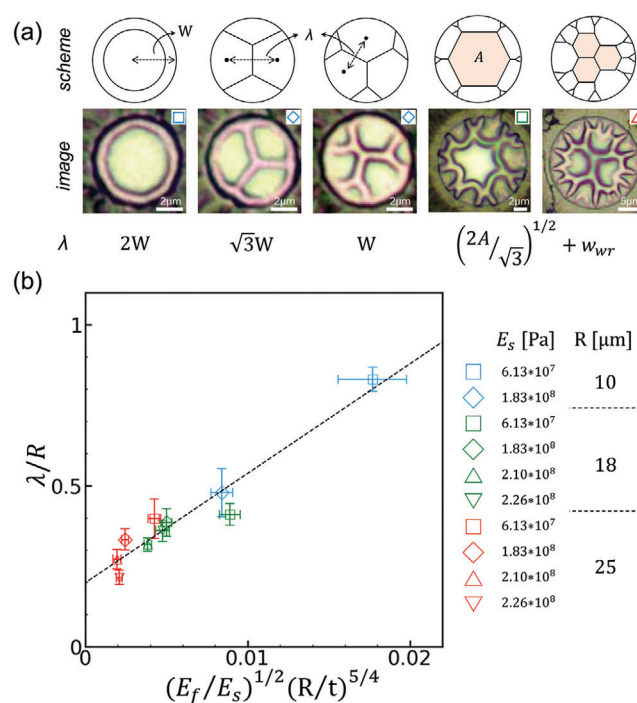

Figure 3. Illustration and representative images outlining the determination of λ for dimple and (part of) buckyball morphologies. b) Relationship between normalized λ/R and $[E_f/E_s)^2(t/R)^5]^{1/4}$. Patterns with an unwrinkled core or cases that do not exhibit a clearly dominant λ were excluded from this plot.

energy expansion as r approaches W, leveraging the established scaling law for the wrinkling cascade $d\lambda/dr \approx \lambda/L$ and $\lambda \sim (W - r)^{1/2}$ from the edge,[35,36,41] we can deduce K_{tens} as follows

$$K_{tens} \sim -\sigma_0(W - r)^{-2} \qquad (8)$$

In light of the nature of scaling relations as approximations rather than exact solutions, assessing all λ values for varying r by comparing K_{tens} with K_{curv} presents certain challenges. However, as K_{tens} diverges when r approaches W, it is apparent that within the region containing the final cascade (closest to the edge), K_{tens} dominates. By defining λ_c and L_c as the wavelength and length of the (final) cascade, respectively, and considering r at the final cascade as $W - L_c$, we can modify Equation (6), along with the approximation $K_{eff} \approx K_{tens}$, as follows:

$$\lambda_c \sim L_c^{0.5} \qquad (9)$$

As depicted in **Figure 4**, experimental findings about the wrinkling cascade align closely with the scaling law. An intriguing observation is that for a fixed W, L_c displays no dependency on E_s, whereas it demonstrates a decreasing trend with an increasing W. This substantiates that $\lambda_c \sim (B/K_{tens})^{1/4}$ is not a function of E_f/E_s or R/t, but rather a function of r/W.

3. Conclusion

In conclusion, our exploration of pattern formation in confined core-shell structures has uncovered several significant insights
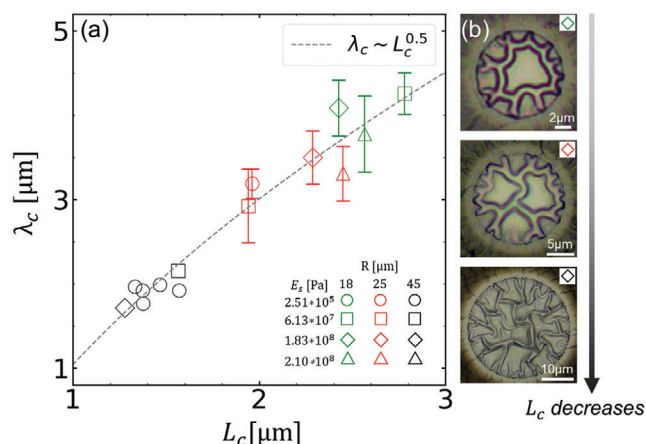
**ADVANCED
SCIENCE NEWS**

www.advancedsciencenews.com

**ADVANCED
MATERIALS
INTERFACES**

www.advmatinterfaces.de

Figure 4. a) Scaling plot and b) representative images demonstrating the relationship between λ_c and L_c.

into their intricate pattern formation behavior. Notable findings include the successful derivation of a tailored α for thermal-induced sheet conformation on a spherical cap-shaped substrate, revealing a fundamental connection between α and L. Importantly, our experimental validation reinforces this correlation, spanning from the conformation of sheets onto liquid substrates to the buckling behavior of core-shell microspheres. Furthermore, we have formulated a new scaling law that precisely computes λ within the bulk region where the edge effect is negligible. This methodology offers a quantitative framework that extends beyond traditional pattern selection using C_s. Furthermore, the inclusion of K_{tens} in the boundary effects has enabled a quantitative investigation of the wrinkling cascade, revealing the correlation between λ_c and L_c, even though the exact solution for $\lambda = \lambda(r)$ remains an unresolved issue. The inquiry related to novel synchronized patterns not only furnishes theoretical guidance but also presents substantial potential for pragmatic utilization across a spectrum of practical domains. For instance, the mechanical properties of the substrates studied in this research closely resemble those of human skin,[44] which can serve as a theoretical basis for body-conformable electronics. Additionally, structures with large deformations adorned with locally tunable hierarchical wrinkled surfaces hold significant potential for optical and photonic applications, such as light harvesting.[45]

4. Experimental Section

Pattern Engineering of Confined Core-Shell Microstructures: A photocurable polyurethane acrylate (PUA, 301RM, Minuta Tech) precursor was blended with ethanol at 1:5 weight ratios. This mixture was then spin-coated onto a cover glass at 3000 rpm for 30 s. Subsequently, a micropillar stamp with diameters of 10, 20, 30, and 100 μm, respectively, was carefully placed onto the spin-coated precursor film. Gentle pressure was applied to the stamp for approximately 10 s before removing it. Afterward, prepolymer droplets were transferred onto the stamp, and the system was allowed to stabilize for approximately 30 min until the droplets reached their equilibrium shape. To control the degree of curing (E_s), UV exposure was applied for a duration ranging from 0 to 100 s. The UV exposure was carried out using a Fusion Cure System (Minuta Tech, MT-UV-A-15) with an intensity of approximately 15 mW cm^{-2} and the band range of 315 to

400 nm, under consistent ambient air conditions. Subsequently, the stabilized microdroplets were loaded into a thermal evaporator, and a 20 *nm* thick layer of aluminum was deposited onto them. This deposition process was conducted under high vacuum conditions ($\approx 10^6$ torr) and at a constant deposition rate of approximately 3 Ås^{-1}. After the metal deposition, the bottom of the transparent substrate was exposed to UV light as a post-processing step to fix the microstructures.

Characterizations: Scanning Electron Microscope (SEM) images were captured using an EM-30 SEM instrument (COXEM, Republic of Korea) operating at an acceleration voltage of 10 kV.

Confocal images were acquired using 3D Surface Confocal Laser Scanning Microscope (Carl Zeiss LSM 800 MAT microscope) with magnifications of X50 and X100.

Optical Microscope (OM) images were obtained through Olympus BX41M. Contact angles were measured using a CAM 200 contact angle meter (KSV Instrument Ltd., Finland).

Young's modulus of the fully cured substrate ($E_{s,fc}$ was measured using a Nano Indenter (Anton Paar Ltd, STeP500 NHT3 and MCT3).

Image Processing: Image processing was performed using the cv2 library in Python, the Image Processing Toolbox in MATLAB, and ImageJ software.

Statistical Analysis: All statistical analyzes were conducted using Python's matplotlib library. The p values were measured by confocal images obtained for each curing time ($\tau = 0, 10, 20, 40, 100$ s), evaluating data from four microstructures at the coordinates (x, y, z) (10^{20} points) raw data and cross-sectional data. The $E_{s,fc}$ values were determined by averaging measurements from five nanoindentation tests and further analyzed using FFT analysis to estimate E_s for each curing time (see Figure S2, Supporting Information). R values were obtained for each OM image using the circle detection tool in the cv2 library and used to evaluate α. λ values were also obtained from the OM images, with 10 to 90 data points per experimental condition. The means and standard deviations of the data were used to create Figure 3. Furthermore, λ_c and L_c were graphically represented in Figure 4, deduced from the mean and standard deviation of the sample of each unit of OM image.

Supporting Information

Supporting Information is available from the Wiley Online Library or from the author.

Conflict of Interest

The authors declare no conflict of interest.

Data Availability Statement

The data that support the findings of this study are available from the corresponding author upon reasonable request.

**ADVANCED
SCIENCE NEWS**

www.advancedsciencenews.com

**ADVANCED
MATERIALS
INTERFACES**

Open Access

www.advmatinterfaces.de

[1] J. Li, P. Yang, X. Li, C. Jiang, J. Yun, W. Yan, K. Liu, H. J. Fan, S. W. Lee, *ACS Energy Lett.* **2022**, *8*, 1.

[2] J. Li, J. Zhao, J. A. Rogers, *Acc. Chem. Res.* **2018**, *52*, 53.

[3] K. R. Jinkins, S. Li, H. Arafa, H. Jeong, Y. J. Lee, C. Wu, E. Campisi, X. Ni, D. Cho, Y. Huang, *Sci. Adv.* **2022**, *8*, eabo0537.

[4] S. Li, H. Xia, X. Sun, Y. An, H. Zhu, H. Sun, *Adv. Funct. Mater.* **2022**, *32*, 2202277.

[5] D. B. Ahn, W. Kim, K. Lee, S. Lee, S. Kim, S. Park, Y. Hong, S. Lee, *Adv. Funct. Mater.* **2023**, *33*, 2211597.

[6] J. Liu, S. Jiang, W. Xiong, C. Zhu, K. Li, Y. Huang, *Adv. Funct. Mater.* **2022**, *32*, 2109214.

[7] P. Giannakou, M. O. Tas, B. L. Borgne, M. Shkunov, *ACS Appl. Mater. Interfaces* **2020**, *12*, 8456.

[8] J. J. Adams, E. B. Duoss, T. F. Malkowski, M. J. Motala, B. Y. Ahn, R. G. Nuzzo, J. T. Bernhard, J. A. Lewis, *Adv. Mater.* **2011**, *23*, 1335.

[9] S. I. Rich, S. Lee, K. Fukuda, T. Someya, *Adv. Mater.* **2022**, *34*, 2106683.

[10] S. I. Rich, Z. Jiang, K. Fukuda, T. Someya, *Mater. Horiz.* **2021**, *8*, 1926.

[11] G. D. Cha, D. Kang, J. Lee, D. Kim, *Adv. Healthc. Mater.* **2019**, *8*, 1801660.

[12] S.-H. Sunwoo, K.-H. Ha, S. Lee, N. Lu, D.-H. Kim, *Ann. Rev. Chem. Biomol. Eng.* **2021**, *12*, 359.

[13] T. A. Witten, *Rev. Mod. Phys.* **2007**, *79*, 643.

[14] J. Hure, B. Roman, J. Bico, *Phys. Rev. Lett.* **2011**, *106*, 174301.

[15] C. Py, P. Reverdy, L. Doppler, J. Bico, B. Roman, C. N. Baroud, *Phys. Rev. Lett.* **2007**, *98*, 156103.

[16] L. Jin, M. Yeager, Y.-J. Lee, D. J. O'Brien, S. Yang, *Sci. Adv.* **2022**, *8*, eabq3248.

[17] H. King, R. D. Schroll, B. Davidovitch, N. Menon, *Proc. Natl. Acad. Sci. U.S.A.* **2012**, *109*, 9716.

[18] F. Box, D. Vella, R. W. Style, J. A. Neufeld, *Proc. R. Soc. A* **2017**, *473*, 20170335.

[19] Y. Timounay, R. De, J. L. Stelzel, Z. S. Schrecengost, M. M. Ripp, J. D. Paulsen, *Phys. Rev. X* **2020**, *10*, 021008.

[20] Y. Timounay, A. R. Hartwell, M. He, D. E. King, L. K. Murphy, V. Démery, J. D. Paulsen, *Phys. Rev. Lett.* **2021**, *127*, 108002.

[21] G. M. Grason, B. Davidovitch, *Proc. Natl. Acad. Sci. U.S.A.* **2013**, *110*, 12893.

[22] J. D. Paulsen, E. Hohlfeld, H. King, J. Huang, Z. Qiu, T. P. Russell, N. Menon, D. Vella, B. Davidovitch, *Proc. Natl. Acad. Sci. U.S.A.* **2016**, *113*, 1144.

[23] B. Davidovitch, Y. Sun, G. M. Grason, *Proc. Natl. Acad. Sci. U.S.A.* **2019**, *116*, 1483.

[24] D. P. Dubal, N. R. Chodankar, D.-H. Kim, P. Gomez-Romero, *Chem. Soc. Rev.* **2018**, *47*, 2065.

[25] W. Gao, H. Ota, D. Kiriya, K. Takei, A. Javey, *Acc. Chem. Res.* **2019**, *52*, 523.

[26] E. Hohlfeld, B. Davidovitch, *Phys. Rev. E* **2015**, *91*, 012407.

[27] S. Liu, J. He, Y. Rao, Z. Dai, H. Ye, J. C. Tanir, Y. Li, N. Lu, *Sci. Adv.* **2023**, *9*, eadf2709.

[28] F. Box, L. Domino, T. O. Corvo, M. Adda-Bedia, V. Démery, D. Vella, B. Davidovitch, *Proc. Natl. Acad. Sci. U.S.A.* **2023**, *120*, 2212290120.

[29] G. Cao, X. Chen, C. Li, A. Ji, Z. Cao, *Phys. Rev. Lett.* **2008**, *100*, 036102.

[30] D. Breid, A. J. Crosby, *Soft Matter* **2013**, *9*, 3624.

[31] N. Stoop, R. Lagrange, D. Terwagne, P. M. Reis, J. Dunkel, *Nat. Mater.* **2015**, *14*, 337.

[32] F. Xu, S. Zhao, C. Lu, M. Potier-Ferry, *J. Mech. Phys. Solids* **2020**, *137*, 103892.

[33] F. Xu, S. Zhao, *Extreme Mech. Lett.* **2020**, *40*, 100860.

[34] E. Cerda, L. Mahadevan, *Phys. Rev. Lett.* **2003**, *90*, 074302.

[35] H. Vandeparre, M. Piñeirua, F. Brau, B. Roman, J. Bico, C. Gay, W. Bao, C. N. Lau, P. M. Reis, P. Damman, *Phys. Rev. Lett.* **2011**, *106*, 224301.

[36] J. Huang, B. Davidovitch, C. D. Santangelo, T. P. Russell, N. Menon, *Phys. Rev. Lett.* **2010**, *105*, 038302.

[37] D. Kang, C. Pang, S. M. Kim, H. S. Cho, H. S. Um, Y. W. Choi, K. Y. Suh, *Adv. Mater.* **2012**, *24*, 1709.

[38] D. Dendukuri, P. Panda, R. Haghgooie, J. M. Kim, T. A. Hatton, P. S. Doyle, *Macromolecules* **2008**, *41*, 8547.

[39] J. W. Hutchinson, *Proc. R. Soc. A* **2016**, *472*, 20160577.

[40] H. G. Allen, *Analysis and design of structural sandwich panels*, Elsevier, Amsterdam **2013**.

[41] S. Deng, V. Berry, *ACS Appl. Mater. Interfaces* **2016**, *8*, 24956.

[42] P. Kim, M. Abkarian, H. A. Stone, *Nat. Mater.* **2011**, *10*, 952.

[43] J. G. Bae, S. H. Sung, H. Lee, K. Char, H. Yoon, W. B. Lee, *Soft Matter* **2016**, *12*, 6507.

[44] A. Kalra, A. Lowe, *J. Mater. Sci. Eng.* **2016**, *5*, 1000254.

[45] J. B. Kim, P. Kim, N. C. Pégard, S. J. Oh, C. R. Kagan, J. W. Fleischer, H. A. Stone, Y.-L. Loo, *Nat. Photonics* **2012**, *6*, 327.